International Journal of Plasticity 197 (2026) 104593

Contents lists available at ScienceDirect

International Journal of Plasticity

journal homepage: www.elsevier.com/locate/ijplas

A micromechanical investigation of plasticity in ordered NbMoCrTiAl and disordered TaNbHfZrTi refractory compositionally complex alloys at room temperature

Jin Wang [a,*], Nicolas J. Peter [a], Martin Heilmaier [b], Ruth Schwaiger [a,c,*]

[a] Institute of Energy Materials and Devices (IMD), Forschungszentrum Juelich GmbH, 52425 Juelich, Germany
[b] Institute for Applied Materials, Karlsruhe Institute of Technology (KIT), 76131 Karlsruhe, Germany
[c] Chair of Energy Engineering Materials, Faculty 5, RWTH Aachen University, 52056 Aachen, Germany

ARTICLE INFO

Keywords:
BCC
B2
Refractory compositionally complex alloy
Micromechanical testing
Dislocation

ABSTRACT

Refractory compositionally complex alloys (RCCAs) are known for their exceptional high-temperature resistance. However, their inherent brittleness at room temperature limits broader practical applications. To explore the effects of microstructure and loading conditions on their deformation behavior, micromechanical experiments, including microbending and micropillar compression tests, were performed on two representative RCCAs: equimolar NbMoCrTiAl (ordered B2 crystal structure) and TaNbHfZrTi (disordered A2 crystal structure). Both alloys demonstrated significant plastic deformation, with strains exceeding 40% at room temperature. Despite prior reports of limited ductility in NbMoCrTiAl at the millimeter scale, our micropillar compression tests on single-crystalline pillars oriented along ⟨1 0 0⟩ and ⟨1 1 0⟩ reveal substantial plasticity. The dominant deformation mechanisms in NbMoCrTiAl were identified as crystallographic slip and cross-slip of screw dislocations. By contrast, TaNbHfZrTi exhibited a broader range of mechanisms, including screw dislocation slip and a high density of non-screw dislocations, accompanied by kink band formation and activation of high-order slip planes, which collectively contribute to its remarkable ductility among the highest reported for body-centered cubic RCCAs. The atomic size mismatch inherent in compositionally complex alloys enhances dislocation mobility, while the random distribution of elements promotes the formation of edge segments, further improving ductility. These findings highlight the critical role of microstructural characteristics in tailoring the deformation behavior of RCCAs for room-temperature applications.

1. Introduction

High temperature metals are of significant interest in material science and engineering. For instance, refractory alloys exhibit structural stability at temperatures above 1500 K (Philips et al., 2020), attributed to the high melting points of refractory elements, such as Nb, Ta, Mo, and W. Despite their excellent high-temperature strength, refractory alloys face challenges, including high density, low oxidation resistance, and room temperature brittleness due to their body-centered cubic (BCC) crystal structure. Balancing high-temperature performance with room-temperature ductility for reliable service of BCC refractory alloys remains a critical and challenging issue to address.

* Corresponding authors.
E-mail addresses: jin.wang@fz-juelich.de (J. Wang), r.schwaiger@fz-juelich.de (R. Schwaiger).

https://doi.org/10.1016/j.ijplas.2025.104593
Received 17 October 2025; Received in revised form 5 December 2025
Available online 29 December 2025

Plastic deformation in BCC materials, including disordered A2 structures and ordered B2 structures (which are made up of two interpenetrating simple cubic lattices, unlike conventional BCC), often relies on the motion of screw dislocations, which is thermally activated. The activation temperature for this process is typically above room temperature (Hirth and Lothe, 1982). In real crystals with preexisting defects, dislocations can move via a kink-pair mechanism. This involves two kinks of opposite signs, or edge segments, connecting the dislocation line, making motion energetically more favorable than the energy required to move a straight dislocation (Seeger, 2022). The separation of the kinks determines the size of the kink-pair, which can be reduced by introducing atoms of different sizes (Maresca and Curtin, 2020) or other lattice defects, hence increasing the density of edge segments . For instance, in a study of the dislocation behavior of a refractory multi-principal element alloy (MoNbTi), a greater variety of dislocation pathways and activation of high-order slip planes were observed due to the globally random structure compared to conventional BCC dilute alloys (Wang et al., 2020a). The presence of multiple alloying elements in compositionally complex alloys increases atomic size misfit and chemical complexity (Li et al., 2019; Sun et al., 2025), which both contribute to strengthening. Moreover, the degree of atomic randomness or ordering (Zhang et al., 2019) of atoms influences the energy landscape and, consequently, the shape, motion, and resistance of dislocations (Li et al., 2025a; Lyu et al., 2025, 2023; Zhai and Zaiser, 2019). This variation in atomic-scale ordering further affects dislocation-mediated deformation at larger length scales, leading to mechanical responses that differ from those of conventional alloys.

We selected two refractory compositionally complex alloys (RCCAs) with comparable atomic size misfit (~5% (Chen, 2020; Thirathipviwat et al., 2022)) but distinct lattice structures for comparison: the A2-structured TaNbHfZrTi alloy, also known as the "Senkov" alloy (Senkov et al., 2011), and the B2-structured NbMoCrTiAl alloy, which contains two additional elements compared to Wang et al. (2020a). The TaNbHfZrTi alloy exhibits exceptional ductility at room temperature (Zherebtsov et al., 2020; Dirras et al., 2016b,a; Lilensten et al., 2018; Chen et al., 2021; Feuerbacher et al., 2015). Previous studies have identified various plastic deformation mechanisms for TaNbHfZrTi, including cross-slip (Charpagne et al., 2022), twinning (Senkov et al., 2011; Wang et al., 2020b), kinking (Zherebtsov et al., 2020; Dirras et al., 2016a; Chen et al., 2021), and shear (Zherebtsov et al., 2020; Dirras et al., 2016b,a), all contributing to its high ductility at room temperature. The NbMoCrTiAl alloy, consisting of five principal elements in equiatomic proportions, was designed to enhance oxidation resistance and mechanical properties, including yield strength and ultimate strength at high temperatures (Chen et al., 2016, 2018, 2021), outperforming the TaNbHfZrTi alloy in these aspects (Feuerbacher et al., 2015). However, compression tests conducted on millimeter sized polycrystalline samples at room temperature revealed no plasticity in this alloy (Chen et al., 2016). Its brittle behavior was attributed to its B2-ordered crystal structure (Chen et al., 2019) and the presence of intermetallic grain boundary precipitates (Müller et al., 2020). Whether the observed brittleness is intrinsic to the B2 structure or predominantly governed by the grain boundary precipitates has not yet been studied systematically. Micropillar compression experiments at the grain boundaries of the NbMoCrTiAl sample (Wang et al., 2024a) revealed that the presence of intermetallic precipitates (also observed in Müller et al. (2020)) contributed to crack initiation and propagation at the grain boundaries. This suggests that the brittleness observed at the millimeter scale may not be mainly attributed to its B2-ordered crystal structure (Chen et al., 2019). Thus, a key question arises: do the distinct crystal structures of TaNbHfZrTi and NbMoCrTiAl inherently dictate their brittleness or ductility? Specifically, would a single crystal behave differently from a polycrystal, considering that most studies have focused on polycrystalline materials? To this end, we conducted a series of micromechanical experiments, including microcompression and microbending tests in individual grains, thereby minimizing the effects of grain boundaries and grain boundary phases.

Previous studies have shown that elements such as Hf, Zr, and Ti contribute to strengthening and plasticity in RCCAs, primarily through their contributions to atomic size misfit (Senkov et al., 2011; Chen et al., 2016). While the deformation behavior of A2-type RCCAs has been widely reported, experimental studies on deformation mechanisms of B2-structured RCCAs remain relatively limited, particularly at small scales where grain boundary effects can be minimized. Given that the two alloys have comparable atomic size misfits but different degrees of ordering, they provide a controlled basis for investigating how chemical randomness influences dislocation activity in BCC systems. Therefore, the goal of this work is to explore how different degrees of atomic ordering, i.e., disordered A2 and ordered B2, affect dislocations and plastic behavior at room temperature in a body-centered cubic structure. By conducting single-crystalline micromechanical experiments combined with microstructural analysis, we aim to understand the intrinsic deformation mechanisms of both ordered and disordered RCCAs, and the role of atomic scale randomness in plasticity under ambient conditions.

2. Materials and methods

Two RCCAs, i.e., TaHfZrNbTi and NbMoCrTiAl, were investigated using microbending and microcompression experiments in order to evaluate plasticity and deformation mechanisms under both tensile and compressive loading. Advanced electron microscopy methods were employed to analyze slip traces and related dislocation behaviors.

2.1. Materials and sample preparation

Fully homogenized specimens of TaHfZrNbTi and NbMoCrTiAl were studied. The two alloys NbMoCrTiAl and TaHfZrNbTi were cast and then homogenized at 1573 K for 20 h and 1473 K for 24 h, respectively. The characteristic material parameters including lattice parameter, atomic misfit, melting and homologous temperatures, etc., are summarized in Table S.1 shown in the Supplementary. Details of the procedures to produce the materials are given elsewhere (Chen et al., 2016, 2018, 2021). The samples were cold-mounted, then ground and gently polished using diamond suspensions. The final polishing step used an OP-A (acidic

alumina) suspension of 0.05 μm grain size to achieve a surface quality suitable for electron backscatter diffraction (EBSD) and micromechanical testing.

Based on the EBSD analysis of the entire sample surfaces using a scanning electron microscope (SEM, Merlin, Zeiss Microscopy, Oberkochen, Germany) equipped with a NordlysNano EBSD detector (Oxford Instruments, High Wycombe, GB), grains of suitable orientation were selected for preparation of microcantilevers and micropillars by focused ion beam milling (FIB, Auriga, Zeiss Microscopy, Oberkochen, Germany).

The samples were prepared to ensure the loading axis is aligned with the ⟨1 0 0⟩ and ⟨1 1 0⟩ crystallographic directions. For the NbMoCrTiAl alloy, which is expected to have an ordered B2 crystal structure, these two directions are reported as the "hard" and "soft" orientations for B2-structured alloys (Miracle, 1993). Similarly, in BCC (A2) crystal structures, these directions are typically selected for micromechanical experiments to study fracture and slip mechanisms, due to the activation of specific cleavage and slip systems (Schmitt, 2016; Riedle et al., 1996; Wang, 2021; Wang et al., 2022).

Microcantilevers with triangular cross sections having an internal angle of the bottom apex of ~50° were fabricated to achieve a width W of ~5 μm and a length-to-width ratio > 6. The microcompression samples were prepared by annular milling to a top diameter d_t of ~5 μm and a height h_p of ~15 μm and with a typical taper angle of 5°. The dimensions of every cantilever and every pillar were determined from SEM images. The sample fabrication is illustrated in Figure S.1 (showing orientation maps of selected grains and FIB-prepared samples with dimensions indicated) in the Supplementary.

2.2. Micromechanical testing

Micromechanical experiments were conducted using two nanoindenters (Nano Indenter XP, MTS Systems Corp., Eden Prairie, MN, USA and FemtoTools FT-NMT04, FemtoTools AG, Buchs, Switzerland) at different constant displacement rates ranging from 5 nm/s to 100 nm/s. For the cantilever bending experiments, a wedge-shaped diamond indenter tip with a wedge length of 10 μm was used, while compression tests were performed with a flat-ended diamond punch tip of 10 μm diameter.

The engineering stress σ_{CL} along the cantilevers with triangular cross section was determined as (Hunt et al., 2015; Armstrong et al., 2009)

$$\sigma_{CL} = \frac{9PL}{Wh^2} \tag{1}$$

with the applied load P, L as the distance between the fixed end of the cantilever and the loading point, and the cantilever thickness h.

According to simple beam theory (Armstrong et al., 2009; Schwaiger and Kraft, 1999), Hooke's law can be applied in the elastic deformation regime. The strain ε_{CL} during elastic bending of a cantilever beam with triangular cross section is given as

$$\varepsilon_{CL} = \frac{3\delta_{CL}h}{4L^2}. \tag{2}$$

with δ_{CL} as the deflection of the cantilever beam. To determine δ_{CL}, the indenter tip displacement δ was corrected to account for penetration of the indenter tip into the material (Ast, 2016; Kupka and Lilleodden, 2012). The set of equations used together with the description of the corrections applied can be found in the Supplementary. As argued in Gabel and Merle (2020), the application of simple beam theory could even be extended to describe low levels of plasticity. Here, we define the offset yield strength at a plastic strain of 0.02%.

For the microcompression experiments, the measured displacement δ was corrected according to Sneddon (1965) and Zhang et al. (2006) to account for elastic deformation of the material underneath the pillar.

$$\delta_P = \delta - \frac{(1-\nu^2)P}{Ed_b}. \tag{3}$$

with δ_P as the displacement of the pillar surface, Poisson's ratio ν of the materials, and the bottom diameter d_b of the pillar (Figure S.1f). The elastic modulus E was determined from nanoindentation experiments (Wang et al., 2024a). For Poisson's ratio ν 0.38 and 0.28 were assumed for alloys TaNbHfZrTi and NbMoCrTiAl, respectively.

The engineering stress σ and strain ε are calculated as

$$\sigma = \frac{4P}{\pi d_m^2} \tag{4}$$

and

$$\varepsilon = \frac{\delta_P}{h_P}. \tag{5}$$

with the pillar diameter d_m measured at half the pillar height h_P (Figure S.1f).

2.3. Microstructural characterization

After the mechanical testing, the deformed microcompression and cantilever beam samples were carefully analyzed by SEM, scanning transmission electron microscopy (STEM) and transmission Kikuchi diffraction (TKD) (AZtecHKL, Oxford instruments, UK). Thin lamellae were prepared from selected pillars and beams using FIB milling. STEM was performed at an acceleration voltage

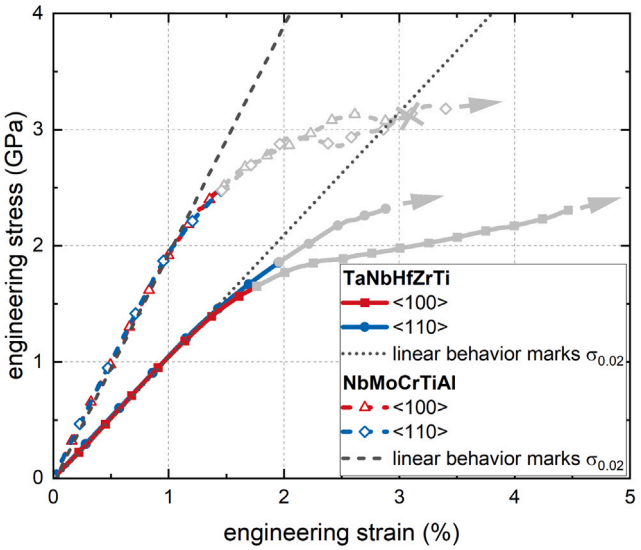

Fig. 1. Representative stress vs. strain behavior of TaNbHfZrTi and NbMoCrTiAl in ⟨1 0 0⟩ and ⟨1 1 0⟩ loading directions determined from microcantilever bending experiments. The data up to 0.2% plastic strain are shown in color. The dashed lines were fitted to the elastic portion of the curves and were shifted to mark the yield points at 0.02% plastic strain ($\sigma_{0.02}$). (For interpretation of the references to color in this figure legend, the reader is referred to the web version of this article.)

of 200 kV and with a semi-convergence angle of 24.7 mrad in an aberration-corrected Titan G2 60–200 CREWLEY microscope (ThermoFischer Scientific, formerly FEI, Netherlands) equipped with a high-brightness field emission electron gun and a Super-X energy-dispersive X-ray spectroscopy (EDS) system. Semi-collection angles of 0–16 mrad for bright field (BF), 31–187 mrad for low angle annular dark field (LAADF) and 69–200 mrad for high angle annular dark field (HAADF) were used. Based on the crystal orientations determined by TKD, the lattice rotation angles and geometrically necessary dislocation (GND) density were determined following the Bunge Euler angle analysis (Wang et al., 2022) and kernel average misorientation (KAM) analysis (Wang, 2021), respectively.

3. Results and discussion

Representative stress–strain curves determined from cantilever bending experiments for the two alloys, i.e., TaNbHfZrTi and NbMoCrTiAl, are shown in Fig. 1. Simple beam theory and, thus, Eqs. (1) and (2) were applied, which can only describe the low-strain regime (shown as colored symbols in Fig. 1). The stress–strain curves at higher strain levels are shown in gray, since this behavior cannot be captured correctly by simple beam theory. The elastic portions of the curves were fitted by straight lines, which were then shifted to mark the yield strength at 0.02% plastic strain. The load vs. deflection curves (Figure S.6 in the Supplementary showing all the curves of bending experiments in this study) vary significantly due to subtle variations of the beam geometries and loading points. For the bending experiments, no pronounced effect of the displacement rate on the deformation behavior was observed.

Higher yield stresses $\sigma_{0.02}$ were observed for NbMoCrTiAl than for TaNbHfZrTi; for the ⟨1 0 0⟩ and the ⟨1 1 0⟩ directions, 1.85 ± 0.31 GPa and 2.18 ± 0.43 GPa, respectively, were determined for NbMoCrTiAl, while the analysis of the TaNbHfZrTi bending experiments gave 1.08 ± 0.08 GPa and 1.45 ± 0.14 GPa, respectively. The yield strength of TaNbHfZrTi is in good agreement with predictions based on the contributions of the atomic size and modulus difference (Senkov et al., 2011). Experimentally, a compressive yield strength of 929 MPa was reported for millimeter sized samples (Senkov et al., 2011). Thus, the size of the cantilevers in our study (~5 μm) has a negligible effect on the measured yield strength of this material. The mean yield stresses obtained here are in a range comparable to nanoindentation results (Wang et al., 2024a). However, NbMoCrTiAl exhibited a notably larger scatter than TaNbHfZrTi. Since the fabrication procedure and geometry of the cantilevers were kept consistent, this scatter likely reflects intrinsic differences in the deformation and fracture behaviors. The deformation characteristics including slip traces and cleavage will be discussed in the following.

Slip traces along ⟨1 1 1⟩ directions on a {1 1 0} plane (top surface of the beam) are observed for both materials and the two cantilever orientations tested (white, dashed lines in Fig. 2). In addition to the ⟨1 1 1⟩ traces, the TaNbHfZrTi-[0 1 0] cantilevers exhibited several slip traces along ⟨2 2 1⟩ (Fig. 2a red arrows and dashed lines), while on the NbMoCrTiAl-[0 1 0] cantilevers ⟨1 1 0⟩ wavy traces (Fig. 2c blue arrows and dashed lines) and on the NbMoCrTiAl-[1 0 1] cantilevers a ⟨1 0 0⟩ line were observed (Figs. 2d and S.2b yellow arrow and dashed lines). With the help of slip traces on the side surfaces of the cantilevers (Figure S.2a), the activated slip system of TaNbHfZrTi-[1 0 1] was identified as the {1 1 2}⟨1 1 1⟩ slip plane families ((1 2 1) and (1 $\bar{2}$ 1) planes), which

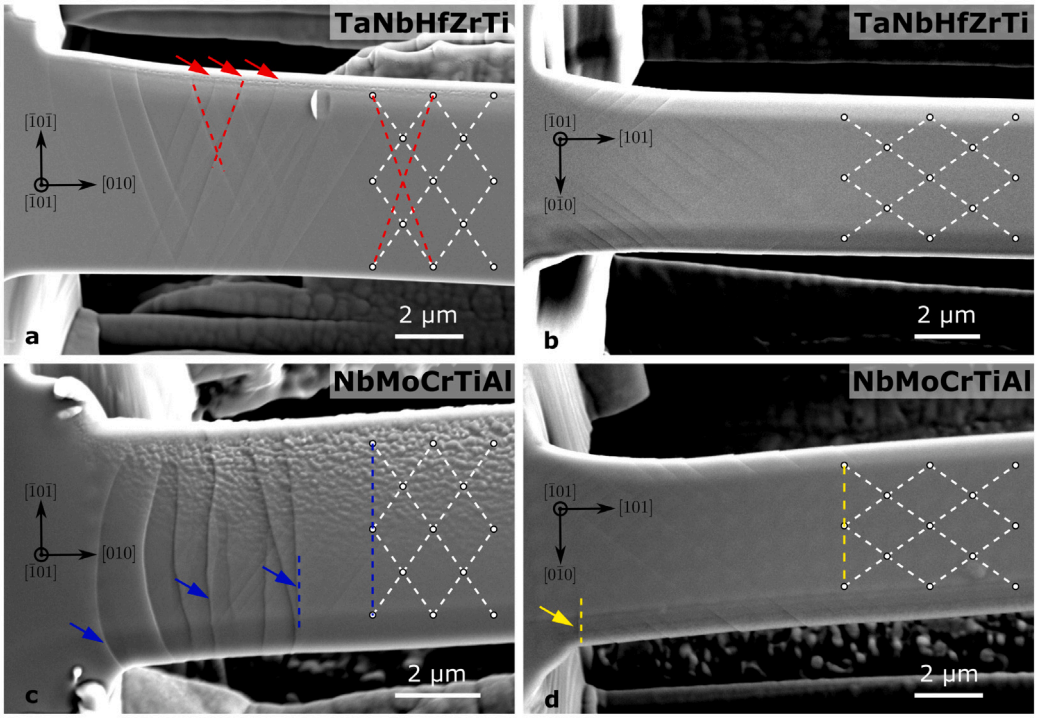

Fig. 2. Slip traces on the top surfaces of the deformed TaNbHfZrTi (a, b) and NbMoCrTiAl (c, d) cantilevers. The cantilevers were prepared to achieve tensile loading along [0 1 0] (a, c) and [1 0 1] (b, d) as indicated by the black arrows with $(\bar{1}\,0\,1)$ surface planes. The slip traces indicated by the white dashed lines are the ⟨1 1 1⟩ directions (a–d), the red lines ⟨2 2 1⟩ (a), the blue lines ⟨1 1 0⟩ (c), and the yellow lines ⟨1 0 0⟩ (d). (For interpretation of the references to color in this figure legend, the reader is referred to the web version of this article.)

agrees well with the predicted maximum resolved shear stress plane (MRSSP) from the Schmid factor calculation (m = 0.471). A detailed analysis of all MRSSPs can be found in the respective section in the Supplementary.

The slip systems observed for the TaNbHfZrTi-[0 1 0] cantilevers were analyzed by LAADF-STEM on the longitudinal cross section (Fig. 3). Two groups of slip lines aligning along ⟨1 1 1⟩ and ⟨2 2 1⟩ orientations were observed in the cross section (Fig. 3a). The traces visible in the cross section and on the cantilever surfaces were highlighted and compared with the schematic of a {1 1 0} plane, with the cross section defined as (1 0 1) and surface as $(\bar{1}\,0\,1)$, respectively. The [$u\,v\,w$] indices of the observed ⟨1 1 1⟩ and ⟨2 2 1⟩ lines were subsequently determined for further slip system analysis. While the ⟨1 1 1⟩ and ⟨2 2 1⟩ lines can in principle span {1 1 0} planes, which are the expected slip planes in BCC materials, in this present case they do not occur in two orthogonal {1 1 0} planes, as observed in the experiment (Fig. 3b). Instead, they exclusively result in {1 3 4} planes. The ⟨1 1 1⟩ traces from the two planes could still be consistent with {1 1 0} planes, but the many ⟨2 2 1⟩ traces strongly indicate the dominant activation of {1 3 4} planes, as shown in Fig. 3b. The {1 3 4} planes are not typically expected to be active in BCC diluted alloys at room temperature, but they have been reported in BCC CCAs (Wang et al., 2020a; Xu et al., 2021; Zhou et al., 2023), where their activation has been associated with non-screw dislocations. While the MRSSP is predicted to be {1 1 2} according to the Schmid factor calculations under [0 1 0] loading (Table S.3 in the Supplementary, listing the Schmid factor of slip planes under the respective loading conditions), the activation of {1 3 4} planes in TaNbHfZrTi cantilevers is likely a combined consequence of random atomic distributions, the complex stress state associated with cantilever bending, and the specific beam geometry. In particular, the chemical fluctuations and lattice distortions arising from the complex atomic distributions in CCAs can effectively affect the dislocation core structure and its surrounding atomic environment, leading to variations in the local slip resistances, i.e., the critical stress required to move a short dislocation line, for different slip planes compared to pure metals (Xu et al., 2021; Romero et al., 2022). Calculated local slip resistances in MoNbTi (Xu et al., 2021) reveal substantial scatter within each slip plane family and reduced differences between the resistances of different slip planes, with some values even overlapping. Consequently, the conventional {1 1 0} and {1 1 2} planes are not necessarily the easiest planes for slip. In MoNbTi, for example, the complex atomic environment can result in easier slip of {1 3 4} planes compared to the other slip systems.

While no fracture was observed in TaNbHfZrTi cantilevers until the maximum deflection set in the experiments was reached, a few of the NbMoCrTiAl cantilevers tested fractured before the maximum deflection was reached (indicated by the cross symbols in Figs. 1 and S.6). However, compared to macro-scale compression experiments on NbMoCrTiAl (Chen et al., 2016), the micro-scale cantilevers exhibited notable plastic deformation as indicated in Fig. 1.

Typical fracture surfaces of NbMoCrTiAl cantilevers are shown in Fig. 4a and b. Both cantilever orientations investigated exhibited fracture. After crack initiation, the crack spread over the cleavage plane, then reoriented along the neutral axis. It then

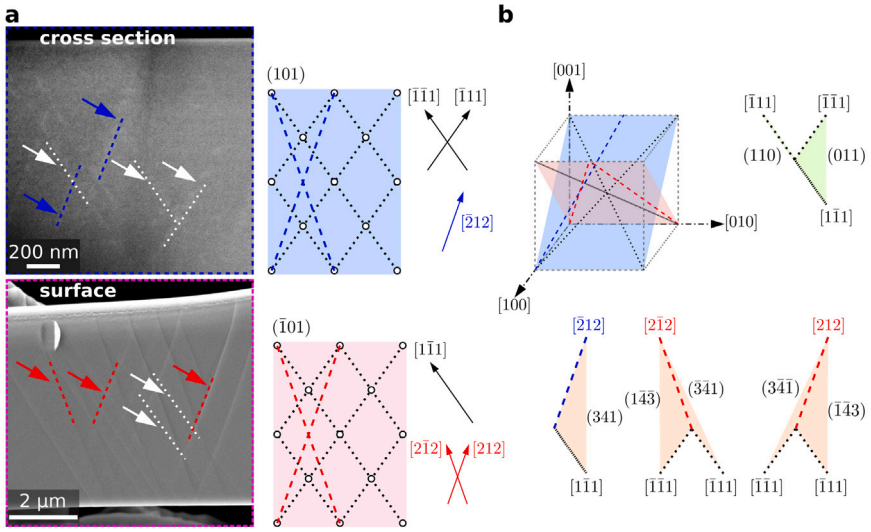

Fig. 3. Slip system analysis comparing slip traces in the longitudinal cross section and on the surface of a TaNbHfZrTi-[0 1 0] cantilever. (a) LAADF-STEM of the cross section and SEM of the cantilever surface with the schematic of a {1 1 0} crystallographic plane. The $(h\,k\,l)$ planes and $[u\,v\,w]$ vectors on each surface are indicated. (b) Schematic of the two orthogonal planes in a unit cell with the observed traces. The possible planes spanned by the ⟨1 1 1⟩ and ⟨2 2 1⟩ traces are shown individually. Planes highlighted in green have a Schmid factor of 0.408 for a ⟨1 1 1⟩ slip direction, and those in nude have a value of 0.453. (For interpretation of the references to color in this figure legend, the reader is referred to the web version of this article.)

propagated through the cross section resulting in final fracture of the beam (Fig. 4c). A schematic is shown in the inset in Fig. 4a. The river lines observed on the crack surfaces are indicative of cleavage fracture for both orientations.

In both Figs. 2c and 4a, wavy ⟨1 1 0⟩ traces were observed (blue arrows) for the cantilever beams loaded along [0 1 0], which are indicative of cross-slip (Caillard et al., 2018; Chen et al., 2024; He et al., 2025; Liu et al., 2025), but were not the starting point of the crack. For the NbMoCrTiAl-[1 0 1] cantilever, ⟨1 0 0⟩ traces (yellow arrow in Figs. 2d, S.2b and c) were associated with a crack with cleavage initiating from this point (yellow arrow in Fig. 4b). The activated slip systems in NbMoCrTiAl and the cleavage planes were determined using the slip traces from the surface and the side surface of the cantilevers (Figs. 4d and S.2b). Accounting for the tilt of the side surface determined from triangular cross section geometry, the slip traces on the side surface were projected on a {1 1 0} plane (i.e., the mid-section of the cantilever) to resolve the crystallographic orientations. As shown in Fig. 4d, the traces on the side surface that connect to the [1 0 1] traces on the surface (blue arrows in Figs. 4a and 3a) align along the [1 1 $\bar{1}$] direction on the ($\bar{1}$ 0 $\bar{1}$) mid-section, and the traces that connect to [1 $\bar{1}$ $\bar{1}$] lines align along the [2 3 $\bar{2}$] direction. By combining these two perpendicular vectors, the crystallographic plane of the ⟨1 1 0⟩ and ⟨1 1 1⟩ traces in Fig. 2c on the NbMoCrTiAl-[0 1 0] sample surface were identified as the ($\bar{1}$ 2 1) and (1 0 1) planes, corresponding to the slip and cleavage planes, respectively (Fig. 4c). For the [1 0 1] cantilevers, slip traces in two directions were identified (Figure S.2b and c). Following the same approach, the cleavage plane was identified as a (1 0 1) plane, and the slip system belongs to the {1 1 0}⟨1 1 1⟩ (case Figure S.2b) and {1 1 2}⟨1 1 1⟩ (case Figure S.2c, same as TaNbHfZrTi-[1 0 1] in Figure S.2a) systems, respectively.

As the MRSSP for both loading directions (Table S.3 in the Supplementary, listing all Schmid factors of the defined loading directions), the {1 1 2}⟨1 1 1⟩ system was identified in TaNbHfZrTi-[1 0 1], NbMoCrTiAl-[0 1 0] and NbMoCrTiAl-[1 0 1] samples. The {1 1 2} slip plane families identified for TaNbHfZrTi and NbMoCrTiAl correspond to typical slip planes of both BCC and B2 materials. The {1 1 0} planes observed with a [1 0 1] tensile axis in NbMoCrTiAl cantilevers are also expected slip planes for the soft orientations in B2 materials (Miracle, 1993). The activation of {1 3 4} slip plane families in TaNbHfZrTi-[0 1 0] samples was unexpected for BCC materials at ambient temperature, however, it has been reported in BCC CCAs as a result of complex atomic distributions (Wang et al., 2020a; Xu et al., 2021). The activation of {1 1 0} planes in NbMoCrTiAl-[1 0 1] and {1 3 4} planes in TaNbHfZrTi-[0 1 0] further indicate that the behavior was not exclusively predicted by Schmid factor. In addition, slip selection in B2 alloys may also depend on the applied stress state and dislocation core structure (La Rosa et al., 2025), making the prediction of active systems more complex. In the TaNbHfZrTi cantilevers, no fracture was observed, whereas some NbMoCrTiAl samples showed cleavage fracture. This difference can be attributed to the compositions of the two RCCAs. Elements such as Hf, Zr, and Ti have been shown in similar CCA systems to lower the ratio of unstable stacking fault energy to surface energy, thereby suppressing cleavage (Wang et al., 2025). Furthermore, the {1 1 0} cleavage planes identified in NbMoCrTiAl are preferred cleavage planes for both hard and soft orientations in conventional B2 materials, due to their low cleavage energy (Miracle, 1993). The simultaneous observation of slip and cleavage traces, which are rarely seen in macroscopic experiments of binary B2 materials, suggests a competition between these mechanisms. The microbending experiments performed on single-crystalline cantilevers to avoid the grain boundary effect and enabled the analysis of plastic deformation behavior, especially for NbMoCrTiAl, which has been reported to exhibit brittleness in polycrystalline samples at the macroscale (Chen et al., 2016).

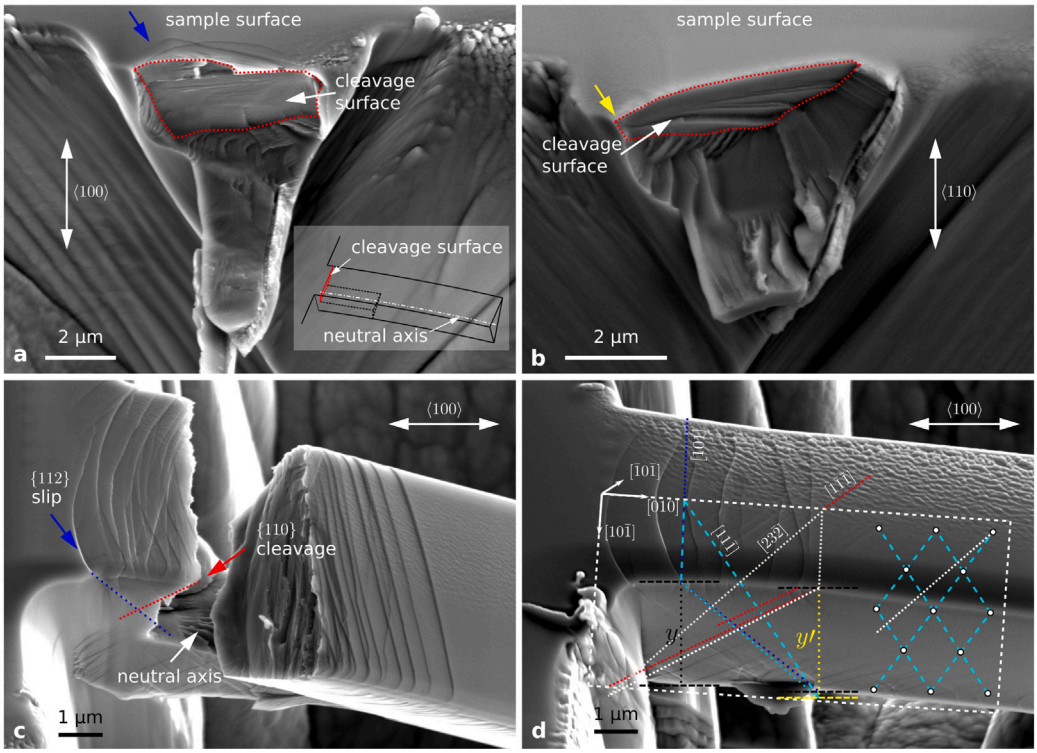

Fig. 4. Fracture surfaces of NbMoCrTiAl cantilevers imaged by SEM for the (a) ⟨1 0 0⟩ and (b) ⟨1 1 0⟩ loading directions. The crack first spread over the cleavage surface (red dotted line), then reoriented along the neutral axis, until the beam finally fractured. The inset in (a) shows a schematic of the cleavage surface (red frame) and the neutral axis (white dashed line) in a deformed beam. The top view in (c) shows the crack reorientation along the plane of the neutral axis. Blue and yellow arrows in (a), (b), (c) mark the slip traces along ⟨1 1 0⟩ and ⟨1 0 0⟩ directions (see Fig. 2), which facilitate the identification of the slip and cleavage systems in (d). The white dashed rectangle in (d) indicates the longitudinal mid-section of the beam showing projections of the crystallographic directions identified. The details of the geometric analysis can be found in the Supplementary, describing the steps for identifications of slip and cleavage systems. Accordingly, traces in (c) were identified as the {1 1 2} slip system (blue line and arrow) and {1 1 0} cleavage plane (red line and arrow). (For interpretation of the references to color in this figure legend, the reader is referred to the web version of this article.)

The compressive stress–strain behavior for the two materials determined by microcompression testing in the two loading directions is shown in Fig. 5. The corresponding load–displacement curves can be found in the Supplementary (Figure S.7 showing all the compression curves). Different displacement rates were applied. For the sake of clarity, for every condition only one curve is shown in color, while the full set of curves is shown in gray.

Compared to the microbending experiments, higher strains reaching more than 40% were observed for both alloys. Up to this level of strain, no cleavage or fracture occurred in any of the pillars. The compressive yield strength – here defined as the stress value at which the stress–strain curve deviates from linear elastic behavior – of TaNbHfZrTi was determined as 1.11 ± 0.04 GPa, and 1.04 ± 0.09 GPa for the ⟨1 0 0⟩ and ⟨1 1 0⟩ loading axis, respectively. While the yield strength values for the ⟨1 0 0⟩ pillars and cantilevers were comparable (1.08 ± 0.08 GPa), the compressive yield strength for the ⟨1 1 0⟩ axis showed a slight difference from the bending experiments, which gave a value of 1.45 ± 0.14 GPa.

The yield strength values from microcompression experiments of NbMoCrTiAl, i.e., 1.41 ± 0.03 GPa for ⟨1 0 0⟩ and 1.16 ± 0.02 GPa for ⟨1 1 0⟩, are significantly lower than the tensile strength values determined from microcantilever deflection.

A clear orientation dependence in the stress–strain behavior can be seen for both alloys, while TaNbHfZrTi additionally shows a pronounced rate-dependent behavior in the ⟨1 1 0⟩ orientation.

The NbMoCrTiAl pillars exhibit orientation-dependent yield stresses but similar stress–strain behavior after yielding at different displacement rates in both orientations. The stress–strain curves of the TaNbHfZrTi ⟨1 0 0⟩ pillars exhibited an almost linear increase after the yield point, which was observed for both displacement rates (red curves in Fig. 5a) without a pronounced rate dependence. For the ⟨1 1 0⟩ loading direction, reduced hardening can be seen (blue curves in Fig. 5a) with distinct behaviors at the different displacement rates. The compressive yield strength values were determined as 1.09 ± 0.09 GPa, 1.03 ± 0.03 GPa, and 0.89 GPa at rates of 50 nm/s, 20 nm/s, and 5 nm/s (corresponding to strain rates of ~5×10^{-3} s^{-1}, ~2×10^{-3} s^{-1}, and ~5×10^{-4} s^{-1}), respectively. At the lower rates of 5 nm/s and 20 nm/s, the stress increases slowly up to a strain of ~15%, and then rapidly until a strain of ~30% is reached (Fig. 5a). At the displacement rate of 50 nm/s, limited hardening can be seen. The different slope of the

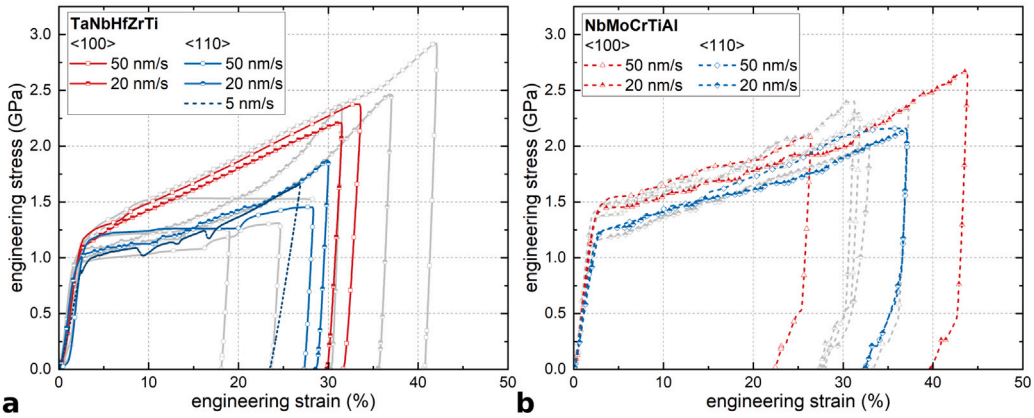

Fig. 5. Stress–strain curves of (a) TaNbHfZrTi and (b) NbMoCrTiAl, as determined by microcompression experiments, were tested for two loading axes (indicated with red and blue colors), corresponding to those used in the microbending experiments, at different displacement rates (shown with different symbols). The reduced unloading slope observed in the 5 nm/s experiment is attributed to variations in experimental conditions, as a displacement-controlled nanoindenter was used for this test, whereas the others employed a load-controlled setup. These differences in unloading behavior are directly related to the distinct configurations of the two experimental methodologies. For every testing condition, one representative curve is shown in color. The load–displacement curves can be found in the Supplementary (Figure S.7 showing all compression curves). (For interpretation of the references to color in this figure legend, the reader is referred to the web version of this article.)

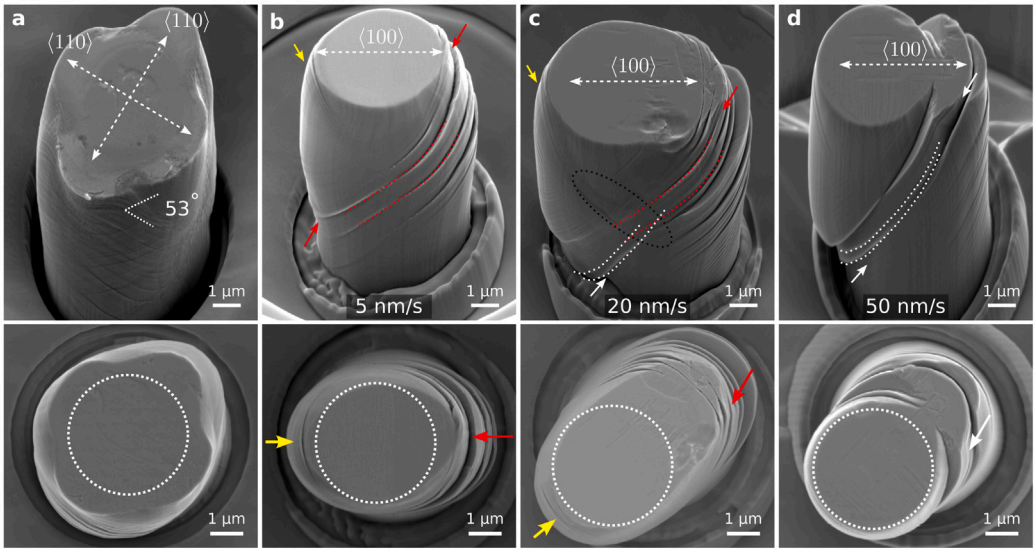

Fig. 6. Side views (top row) and top views of TaNbHfZrTi pillars after microcompression: (a) ⟨1 0 0⟩, 20 nm/s, compressive strain ~40%; (b) ⟨1 1 0⟩, 5 nm/s, compressive strain ~30%; (c) ⟨1 1 0⟩, 20 nm/s, compressive strain ~35%; and (d) ⟨1 1 0⟩, 50 nm/s, compressive strain ~30%. For the side views, the stage tilt angle of 40° was corrected. The white dotted circles in top views mark the original top surface of the pillars before the compression experiment. The crystal orientations indicated by the white dashed arrows in (a), (b), (c), and (d) were determined by EBSD prior to the experiments. The white, yellow and red arrows and lines mark slip traces along different crystallographic orientations, and the black dotted ellipse marks the transition region. (For interpretation of the references to color in this figure legend, the reader is referred to the web version of this article.)

unloading curve after loading at a displacement rate of 5 nm/s is related to the use of different indenters and the different unloading conditions. The distinct rate-dependent stress–strain curves of the TaNbHfZrTi ⟨1 1 0⟩ pillars suggest differences in the underlying deformation behavior, and the corresponding mechanisms were analyzed in detail using SEM and TEM. The deformation features shown in Fig. 6 can be correlated with the loading curves and likely reflect the presence of different deformation mechanisms.

For the TaNbHfZrTi-⟨1 0 0⟩ pillars, the stress–strain curves are identical at slow and fast displacement rates. During compression the material deforms homogeneously along two ⟨1 1 0⟩ directions (dashed arrows in Fig. 6a) resulting in a "four-leaf-clover" shape of the surface (Fig. 6a). Fine lines were observed on the side surface, which were identified as traces of the symmetrical {1 1 2}

slip plane families due to the specific angle of the {1 0 0} planes (i.e., 53°, dotted lines in Fig. 6a). The uniform and continuous deformation along the compression axis reflects the linear increase of the stress–strain curve shown in Fig. 5a.

By contrast, for the ⟨1 1 0⟩ orientation, the material deforms along only one ⟨1 0 0⟩ direction (dashed arrows in Fig. 6b to d). For the displacement rates of 5 nm/s, 20 nm/s, and 50 nm/s, different deformation features were observed.

At displacement rates of 5 nm/s and 50 nm/s, diagonal slip traces were observed on the side surfaces of the pillars (red and white arrows in Fig. 6b and d). These traces were outlined by the dotted lines, they formed two groups with different angles in the slowly and quickly compressed samples. In top view, the traces intersect along the ⟨1 0 0⟩ direction on the deformed pillar surfaces. At a displacement rate of 20 nm/s, both sets of traces appeared on the top and bottom of the pillars' side surfaces, following the two groups of traces (red and white lines in Fig. 6c, taken from Fig. 6b and d). A transition zone between these two regions is visible (dotted ellipse in Fig. 6c). At lower displacement rates, an additional set of parallel traces was observed, contributing to further expansion of the pillar along the ⟨1 0 0⟩ direction (indicated by the yellow arrow in Fig. 6b and c). These distinct differences resulting in very different deformed pillar geometries can, thus, explain the variation in the hardening behaviors shown in Fig. 5.

For further analysis of the active deformation mechanisms in the TaNbHfZrTi micropillar, a cross-sectional thin lamella was prepared for STEM and TKD analyses from the mid-section of a pillar compressed at 20 nm/s to ~30% strain (comparable to Fig. 6c). The out-of-plane orientation of the lamella was close to ⟨1 1 0⟩ (defined as (1 0 1) for further slip system analysis). The STEM images, TKD analysis, and GND density distribution are shown in Fig. 7.

The atomic resolution STEM and the corresponding Fast Fourier Transform (FFT) analysis (Fig. 7d) confirm the BCC (A2) structure of the TaNbHfZrTi sample. Different groups of deformation features can be seen in the cross section. In the upper-left section of Fig. 7a, straight lines were observed aligning at a 45° angle (Fig. 7b), which correspond to the traces appearing at lower rates (Fig. 6b and c, indicated by the yellow arrow). These lines cannot be assigned to any of the known BCC slip systems. They were identified as non-crystallographic slip, denoted by $\{h\,k\,l\}$ (Hirth and Lothe, 1982), which typically occurs at high temperatures or low strain rates. Similar non-crystallographic slip behavior was observed in this alloy (Charpagne et al., 2022). It has been suggested (Hirth and Lothe, 1982) that such non-crystallographic slip is associated with cross-slip between complex slip planes, as the stress required to move a dislocation for {1 1 2} or {1 1 0} slip changes rapidly with varying velocities and temperatures. Additionally, the wavy bands near the 45° lines (highlighted by triangles in Fig. 7b) further indicate cross-slip behavior (Hirth and Lothe, 1982; Caillard et al., 2018; Liu et al., 2025; He et al., 2025): typical changes in direction were observed in a wavy slip trace (Figure S.4), indicating that different slip planes are involved (Caillard et al., 2018).

The lattice rotation distribution determined from the TKD analysis indicates that the significant rotation is in-plane (Figs. 7g and S.5). In the center of the deformed pillar, distinct kink bands (Zherebtsov et al., 2020; Chen et al., 2021; Cook et al., 2024; Hagihara et al., 2016) were observed, as indicated by the lattice rotation map (Fig. 7g) and the orientation maps (Fig. 7h). They are also visible in the STEM images (Fig. 7a and c) and on the pillar side surface (dotted ellipse in Fig. 6c) and are accompanied by two groups of slip traces. According to Li et al. (2025b), the formation of kink bands has been attributed to the Hf content in the alloy. They are usually formed to accommodate the slip of edge dislocations on different glide planes (Cook et al., 2024). The kink bands were identified along a ~45° angle connecting the two regions of opposite lattice rotation directions, localized at the lower left to upper right of the cross section (Fig. 7c and g). The angles to the horizontal of the lines in these two regions were determined as 54.7° (bottom left, white dashed lines in Fig. 7a) corresponding to $[\bar{1}\,1\,1]$ (Fig. 7b and c), and 35.3° (top right, red dashed lines in Fig. 7a) corresponding to $[\bar{1}\,2\,1]$ (Fig. 7c, e, and f). These traces can also be seen on the deformed surface as marked by the white and red lines and arrows in Fig. 6b, c, and d. Detailed analysis of the traces can be found in the Supplementary (Table S.2 listing all intersecting traces of slip planes on a (1 0 1) plane).

Based on the crystallographic orientation, the $[\bar{1}\,1\,1]$ traces are most likely slip lines from the $(1\,2\,\bar{1})[\bar{1}\,1\,1]$ slip system, which corresponds well to the MRSSP (Table S.3 in the Supplementary summarizing the Schmid factor of slip planes under defined loading conditions). The $[\bar{1}\,2\,1]$ traces (red arrows in Fig. 7e), on the other hand, appear more consistent with dense dislocation lines: at higher magnification (Fig. 7e and f), multiple dislocations aligned along the $[\bar{1}\,2\,1]$ directions are observed, including both long segments (Fig. 7e) and short segments (Fig. 7f). The kinked and wavy dislocation segments in Fig. 7e resemble those described in earlier studies (Li et al., 2025a; Maresca and Curtin, 2020) and are attributed to the global atomic randomness of this alloy. These dislocations cannot be of pure screw type, because the projections of pure screw dislocations with ⟨1 1 1⟩ line vectors on the (1 0 1) plane align along either ⟨0 1 0⟩ or ⟨1 1 1⟩ directions. Given that the line vector of the dislocations is $[\bar{1}\,2\,1]$, they are either mixed dislocations with a Burgers vector of $a/2[\bar{1}\,1\,1]$ or edge dislocations with a Burgers vector of $a/2[1\,1\,\bar{1}]$ on the (1 0 1) plane. Furthermore, the short segments with nearly uniform spacing shown in Fig. 7f are consistent with the theoretical description of kinks spaced by a characteristic length (Maresca and Curtin, 2020). The presence of non-screw dislocations and high density of kink-like short segments, together with the observed kink bands, strongly suggest the presence of edge segments in this region.

Strong lattice rotations and a high GND density were observed in the kink band region, whereas these features were less pronounced within the slip bands (Figure S.5), consistent with previous experimental and computational findings (Jouybari et al., 2025). Surrounding the slip band, clear boundaries of a higher dislocation concentration were observed in the TKD analysis and the GND density map (Figure S.5b) indicating the formation of low angle grain boundaries (LAGBs) due to the plastic deformation. By identifying the deformation features in the cross section, the underlying mechanisms including screw dislocation slip (at higher rates), non-screw dislocation activity (at lower rates), and kink band formation (accommodating different slip systems) can be correlated with the surface morphologies of the deformed pillars. Together, these mechanisms explain both the rate-dependent stress–strain curves and the rate-dependent deformation characteristics observed on the deformed pillar surfaces of TaNbHfZrTi ⟨1 1 0⟩.

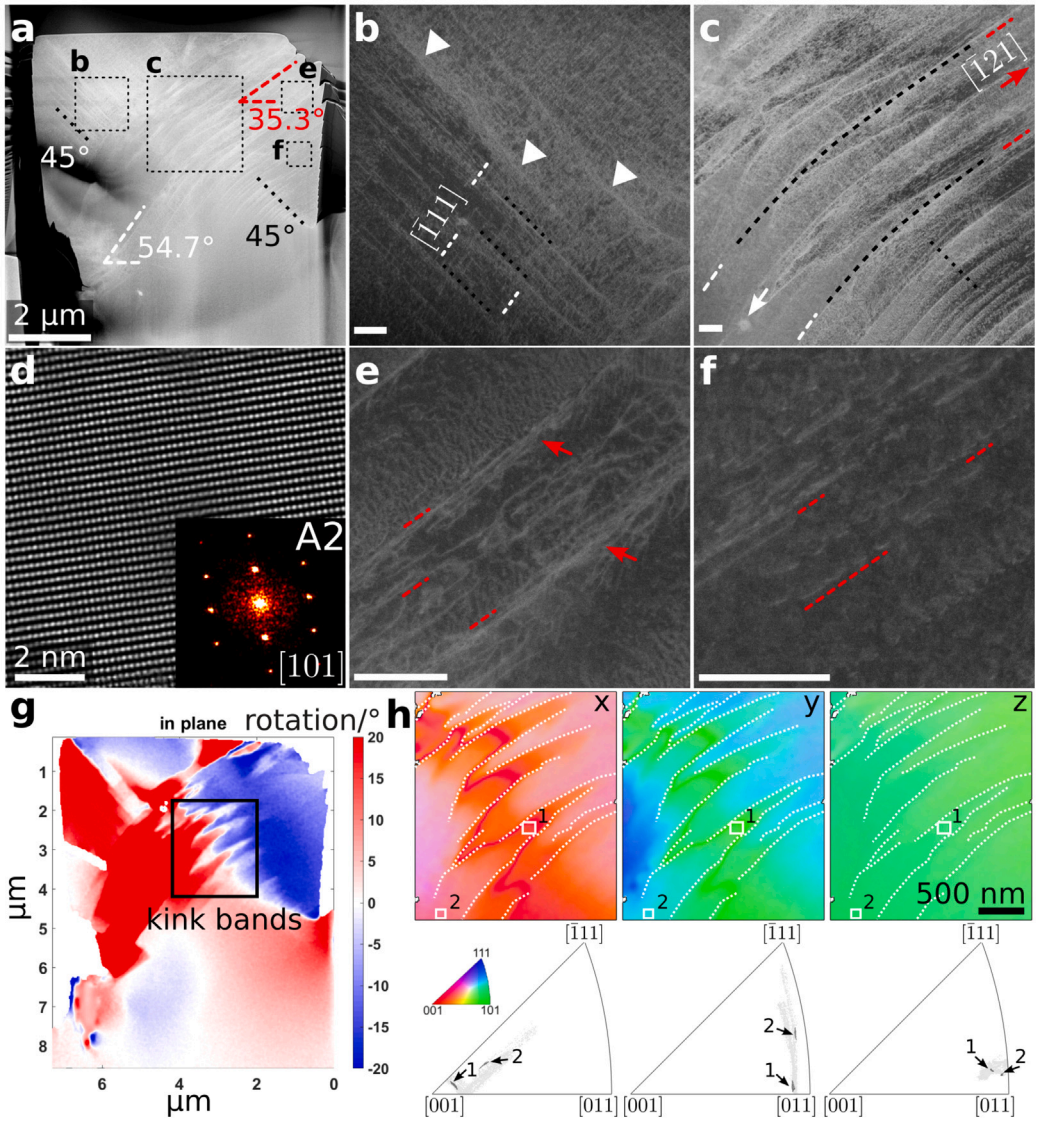

Fig. 7. LAADF-STEM analysis reveals the different deformation mechanisms active during microcompression experiments of TaNbHfZrTi (loading direction ⟨1 1 0⟩, displacement rate 20 nm/s). (a) Overview of the cross section showing the slip systems identified. The regions highlighted by the frames are shown at higher magnification in (b), (c), (e), and (f). Straight lines at angles of 35.3° and 54.7° correspond to the crystallographic directions [$\bar{1}$ 1 1] and [$\bar{1}$ 2 1], respectively. Dotted lines indicate the 45° angle to the loading direction. (b) The black dotted lines correspond to the 45°-lines in (a), while the white dashed lines indicate the [$\bar{1}$ 1 1] direction. The wavy bands are highlighted by the white triangles. (c) White and red dashed lines indicate the [$\bar{1}$ 1 1] and [$\bar{1}$ 2 1] direction, respectively. (d) Atomic resolution STEM image showing the pillar's single-crystalline structure with the corresponding Fast Fourier Transform as inset. (e) and (f) Red dashed lines indicate the [$\bar{1}$ 2 1] direction. The red arrows in (e) indicate the [$\bar{1}$ 2 1] traces, which are also visible at lower magnifications in (a) and (c). The scale bars in (b), (c), (e), and (f) denote 200 nm. (g) The lattice rotation angle map shows the in-plane distribution and opposite rotation directions of two different regions and connected by the kink bands. The inverse pole figure (IPF) maps of the kink band region (highlighted by the frame in (g)) are shown at higher magnification in (h). The white dashed lines indicate the boundaries of each band. Two subregions 1 and 2 confirm the lattice rotation in a kink band as indicated by the IPF triangles. (For interpretation of the references to color in this figure legend, the reader is referred to the web version of this article.)

In the case of NbMoCrTiAl pillars, no significant rate dependence of the stress–strain behavior was observed. However, the yield strength of the ⟨1 0 0⟩ pillars was significantly higher than the yield strength of the ⟨1 1 0⟩ pillars (i.e., by ~35%) (Fig. 5b), while the deformation behavior appears to be independent of the orientation of the loading axis. After the yield point, the slope of the stress–strain curve increases steadily, and the shape of the curves was comparable for all pillars tested.

The deformed pillars were analyzed by SEM (Fig. 8), which did not reveal any significant differences between the different orientations and displacement rates. The material deformed along a single orientation, specifically along ⟨1 1 0⟩ for the ⟨1 0 0⟩ loading

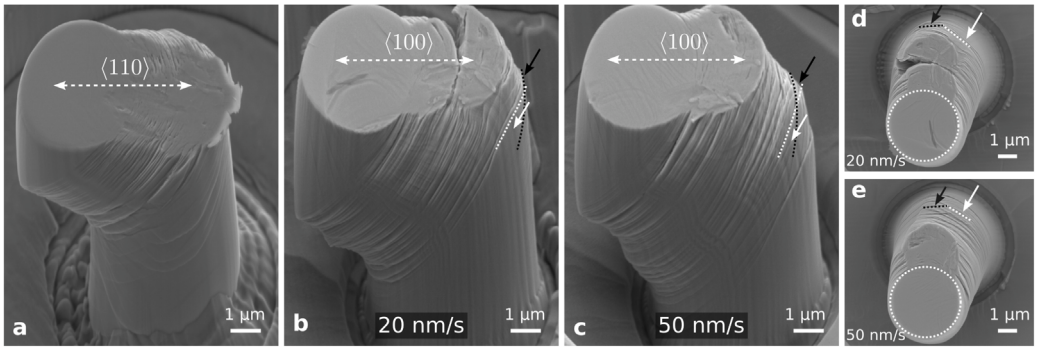

Fig. 8. NbMoCrTiAl pillars after microcompression: (a) loading axis along ⟨1 0 0⟩, deformed at a displacement rate 20 nm/s to a strain of ~30%, (b) loading axis along ⟨1 1 0⟩, deformed at a displacement rate 20 nm/s to a strain of ~35%, and (c) loading axis along ⟨1 1 0⟩, deformed at a displacement rate of 50 nm/s to a strain of ~35%. Top views of (b) and (c) are shown in (d) and (e), respectively. For the side views, the stage tilt angle of 40° was corrected. The white dashed circles in (d) and (e) indicate the original top surface of the pillars before testing. The crystal orientations were determined by EBSD prior to the microcompression experiments.

Table 1
Mechanical properties and activated slip planes of TaNbHfZrTi and NbMoCrTiAl RCCAs.

RCCAs	Loading direction	$\sigma_{0.02}$/GPa, slip plane	$\sigma_{y,c}$/GPa, slip plane
TaNbHfZrTi	⟨1 0 0⟩	1.08 ± 0.08, {1 3 4}	1.11 ± 0.04, {1 1 2}
	⟨1 1 0⟩	1.45 ± 0.14, {1 1 2}	1.04 ± 0.09, {1 1 2}&{1 1 0}&{h k l}
NbMoCrTiAl	⟨1 0 0⟩	1.85 ± 0.31, {1 1 2}	1.41 ± 0.03, cross-slip
	⟨1 1 0⟩	2.18 ± 0.43, {1 1 2} or {1 1 0}	1.16 ± 0.02, {1 1 2}&{1 1 0} cross-slip

axis (dashed line in Fig. 8a), and along a ⟨1 0 0⟩ orientation when the pillars were loaded along ⟨1 1 0⟩ (dashed lines in Fig. 8b and c). In each case, a set of parallel lines was visible on the side surfaces, reflecting the continuous stress increments shown in Fig. 5b. However, multiple slip plane families were activated, as indicated by another set of slip traces on the other sides (white and black lines and arrows in Fig. 8b–e). Similar intersections of different trace groups were also observed on the ⟨1 0 0⟩ pillar (Fig. 8a).

A cross-sectional STEM lamella was prepared from the mid-section of a NbMoCrTiAl compressed pillar for analysis of the deformation mechanisms involved. For comparison with the TaNbHfZrTi sample shown in Fig. 7, we analyzed the NbMoCrTiAl pillar with the same loading direction along ⟨1 1 0⟩ and a displacement rate of 20 nm/s (same pillar as shown in Fig. 8b and d).

STEM and EDS analyses of the NbMoCrTiAl pillar are presented in Fig. 9. The ordered B2 structure of the NbMoCrTiAl alloy was confirmed by HAADF-STEM and FFT analysis (Fig. 9d). Compared to the TaNbHfZrTi alloy in Fig. 7, the deformation characteristics of the NbMoCrTiAl alloy appear more straightforward. One set of slip lines was observed crossing the pillar in diagonal direction, aligning along the $[\bar{1}\,1\,1]$ direction (white arrows in Fig. 9 mark the ⟨1 1 1⟩ directions). However, as seen in Fig. 8b–e, these parallel slip lines belong to two distinct slip plane families, and they appear alternately on the (1 0 1) cross section. At higher magnification, the morphology of the parallel lines changes (e.g., upper-left corner in Fig. 9b, long, straight lines and short, dense curves), suggesting the projection of dislocations from different slip planes. The dislocation lines are generally straight and smooth, and no wavy segments – similar to those observed in TaNbHfZrTi alloy – were detected (Fig. 7e). Several parallel, short defects were observed between the $[\bar{1}\,1\,1]$ lines (Fig. 9e), indicating the cross-slip of screw dislocations (Chou et al., 1987). Additionally, slip lines and a characteristic dislocation jog crossing two symmetrical slip plane families are visible at higher magnification in Fig. 9c and f.

Finally, STEM-EDS analysis shows the presence of a Ti-rich precipitate in the single-crystalline pillar (Fig. 9g and h) as well as cracks as indicated by the red arrows in Fig. 9g. Other deformation characteristics such as non-crystallographic slip and kink bands were not observed.

The analysis of the slip planes associated with the parallel slip lines was performed alongside an examination of the slip traces on the deformed pillar surface, as shown in the Supplementary (Figure S.3) showing a schematic of the slip planes in the pillar and illustrating the traces on the surface. The intersections on the (0 1 0) surface were identified as [0 0 1] and [1 0 1], respectively. Based on this, the two activated slip planes responsible for the parallel $[\bar{1}\,1\,1]$ lines observed on the (1 0 1) TEM cross section and enabling the cross-slip behavior were determined to be the $(\bar{1}\,\bar{1}\,0)$ and $(1\,\bar{2}\,1)$ planes. These planes are highlighted in green and purple in the schematic in Figure S.3. Intersecting slip traces were also observed on the ⟨1 0 0⟩ pillars, but their positions appeared rather random on the curved surface, making them difficult to identify reliably.

The tensile yield stress $\sigma_{0.02}$ from microcantilever bending experiments, compressive yield stress $\sigma_{y,c}$, and the corresponding activated slip planes are summarized in Table 1.

Several key points can be recognized in Table 1: TaNbHfZrTi (A2) exhibits relatively small differences in yield stresses between bending and compression, particularly for the ⟨1 0 0⟩ orientation where the yield stresses are almost identical. By contrast, NbMoCrTiAl (B2) exhibits consistently higher and more scattered $\sigma_{0.02}$ (from bending experiments) compared to the compressive

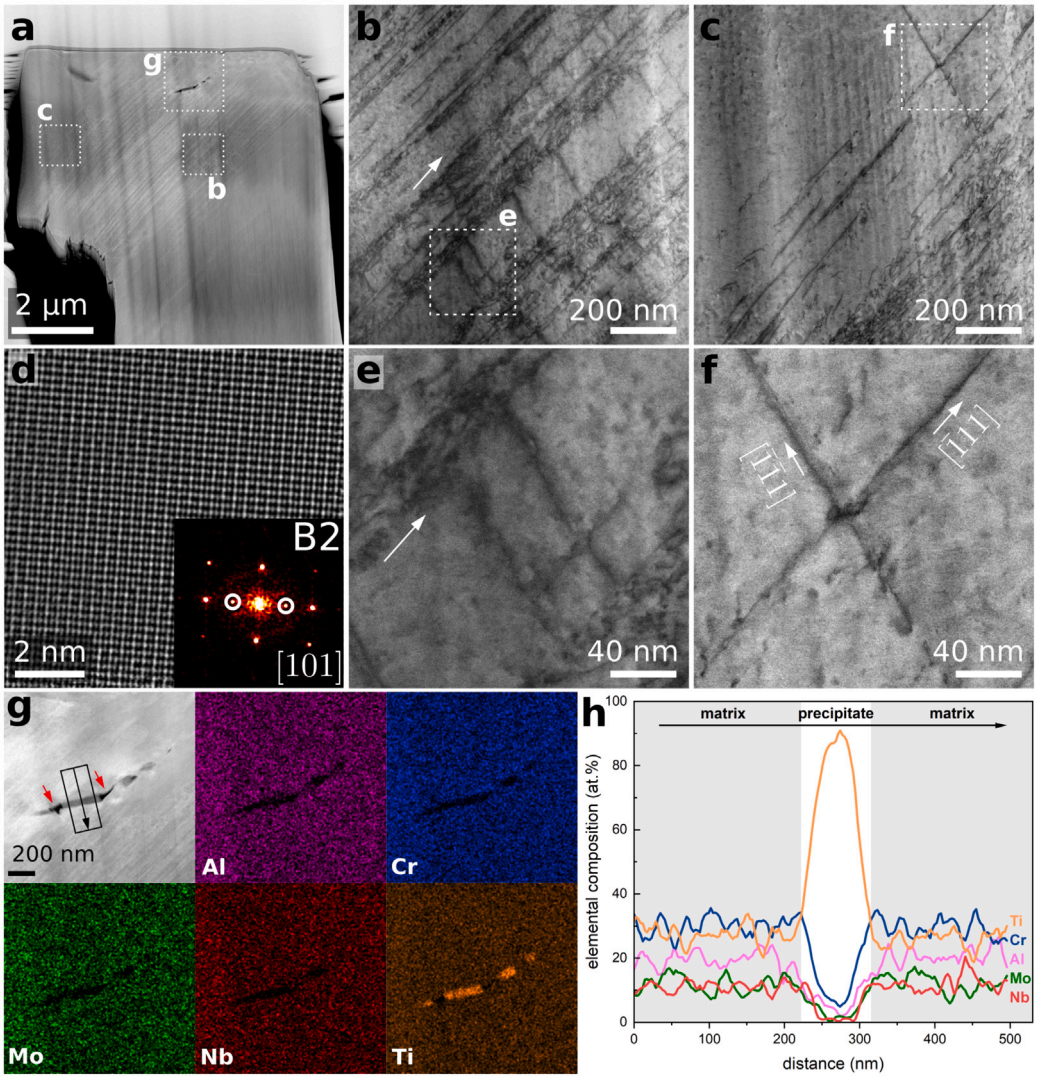

Fig. 9. STEM images of the NbMoCrTiAl-⟨1 1 0⟩ pillar cross section (compressed at 20 nm/s) reveal the deformation microstructures (a–f). The regions marked by the frames in the LAADF-STEM micrograph in (a) are shown at higher magnification (BF-STEM) in (b) and (c), in each with a further magnified region shown in (e) and (f). HAADF-STEM in (d) with the corresponding FFT analysis as inset confirms the B2 structure of NbMoCrTiAl (superlattice reflections are highlighted by white circles). (g) STEM-EDS analysis conducted in the framed region in (a) shows the elemental concentrations, while an integrated line profile extracted across a precipitate (black arrow with integration width) is shown in (h). The precipitate consists almost exclusively of Ti. (For interpretation of the references to color in this figure legend, the reader is referred to the web version of this article.)

yield stresses for both ⟨1 0 0⟩ and ⟨1 1 0⟩, together with variations in the activated slip planes and significant cross-slip during compression. These trends reveal a tension–compression asymmetry, which is particularly evident in the {1 1 2}-dominated cases. Details of the observed behaviors, mechanisms, and dislocation activities will be discussed in the following part.

For the deformation behavior of the TaNbHfZrTi alloy, both bending and compression tests demonstrate significant plasticity after yielding, with yield strengths comparable to the macroscopic results reported in Senkov et al. (2011). As observed in previous studies (Senkov et al., 2011; Chen et al., 2016), this alloy exhibits ductility at both macro- and micro-scales at room temperature. This macroscopic ductility is typically attributed to its homogeneous, single-phase BCC structure and the random distribution of different atoms.

Micro-mechanical experiments, performed with controlled loading rates and orientations within single crystalline grains, provide valuable insights into the deformation mechanisms of the alloy. While the yield strengths remain consistent across various displacement rates and orientations, the plastic deformation behaviors exhibit significant differences. In most loading conditions, slip is dominated by a single slip plane family, including higher-order slip planes. By contrast, during compression along the ⟨1 1 0⟩ axis at lower strain rates, various deformation features are noted, including slip bands associated with dislocation glide on the {1 1 2}

planes, non-crystallographic slip, cross-slip, dense non-screw dislocations, and kink bands that accommodate variations in slip planes such as {1 1 2} (screw dislocation type) and {1 1 0} (non-screw type). These phenomena, particularly the dense edge segments, are uncommon in other BCC dilute materials at room temperature and emphasize the remarkable ductility of the BCC TaNbHfZrTi system under these conditions (Zherebtsov et al., 2020; Charpagne et al., 2022; Dirras et al., 2016a; Chen et al., 2021). A high density of edge or mixed dislocations has also been reported recently in RCCAs with similar compositions, including Ti–Hf–Nb–V–W (Huang et al., 2024), Ti–Zr–Hf–Nb (Wang et al., 2024c), Ti–Zr–Hf–Nb–Mo system (Li et al., 2025b), and NbTaTiHf (Cook et al., 2024) at ambient and elevated temperatures. Calculations of local slip resistances show that, with increasing chemical complexity, both the differences between the slip resistances of different slip planes and the ratio of screw-to-edge become significantly reduced (Xu et al., 2021; Romero et al., 2022; Wang et al., 2024b). This indicates that the preferential activation of low-order slip planes and the dominance of screw dislocation glide, typical of pure BCC metals, are no longer predominant in CCAs. The experimentally observed high density of non-screw dislocations and the activation of higher-order slip planes at room temperature can therefore be attributed to the random distribution of atoms with different sizes (Maresca and Curtin, 2020; Baruffi et al., 2022). This characteristic could explain the relatively lower compressive stress observed in ⟨1 1 0⟩ samples compared to bending experiments, as well as the strength reduction at elevated temperatures in the TaNbHfZrTi alloy.

By contrast, the NbMoCrTiAl RCCA displays no plasticity at the macro-scale, a characteristic attributed to intermetallic precipitates at grain boundaries (Müller et al., 2020) and the ordered B2 structure within grains (Müller et al., 2020; Chen et al., 2019). In micro-mechanical experiments, B2 NbMoCrTiAl samples exhibit reduced plasticity compared to the TaNbHfZrTi system. Nonetheless, notable plastic deformation is observed in both bending and compression tests, which is uncommon for a B2 material (Chen et al., 2016; Yoo and Fu, 1992). Microbending experiments show higher yield strength and greater scatter compared to compression tests, with the average values aligning well with hardness measurements obtained from nanoindentation (Wang et al., 2024a). In bent samples, slip and cleavage traces are evident, with some cantilevers ultimately failing through cleavage fracture. The larger scatter in $\sigma_{0.02}$ can likely be attributed to the competition between slip and cleavage mechanisms. For both ⟨1 0 0⟩ and ⟨1 1 0⟩ loading directions, the {1 1 0} plane serves as the primary cleavage plane, consistent with expectations for B2 materials (Yoo and Fu, 1992).

In microcompression experiments, {1 0 0} grains (considered the hard orientation for B2 materials (Miracle, 1993)) exhibit higher yield strength. Similar stress–strain behavior is observed in the plastic regime across different displacement rates and orientations. In compressed samples, strain levels exceeding 40% are achieved without pillar fracture. Dense slip lines, including intersecting slip planes and cross-slip behavior, are observed diagonally across the pillars. Many dislocations of screw character (long, straight lines) align with these slip lines, indicating sustained plastic deformation. The observed plastic deformation features are independent of orientation or loading rate, suggesting that dislocation slip is the primary deformation mechanism.

No significant edge segments were observed in the NbMoCrTiAl samples, even though this B2 alloy has an atomic size misfit comparable to TaNbHfZrTi (Chen, 2020; Thirathipviwat et al., 2022). Previous numerical studies on the correlation between edge dislocation fractions and atomic size misfit have mostly focused on disordered materials (Baruffi et al., 2022) or short range order (Antillon et al., 2021). More recently, Li et al. (2025a), Lyu et al. (2023) statistically investigated the relationship between dislocation shape and chemical randomness, revealing a transition from wiggling to smooth dislocation lines with increasing ordering, attributed to the decreasing athermal dislocation energy fluctuations. While dislocation shape is governed by the local potential energy landscape, chemical randomness has a more significant influence than the average atomic size misfit, which usually characterizes the overall atomic environment. Our experimental observations, obtained from direct comparisons of dislocation shapes in A2 and B2 alloys, align well with these theoretical interpretations. These indicate that atomic ordering affects the energy landscape, thereby influencing dislocation pathways and the dislocation type.

Anisotropic plastic behavior is observed when comparing the yield stresses in microbending and microcompression experiments for both ⟨1 0 0⟩ and ⟨1 1 0⟩ loading directions. This anisotropy includes both orientation dependence, as reflected for example by the different compressive stresses of the B2 alloy, and tension–compression asymmetry. The latter is mostly evident in the {1 1 2} dominated TaNbHfZrTi-[1 0 1], NbMoCrTiAl-[0 1 0], and NbMoCrTiAl-[1 0 1] samples, where significantly lower compressive stresses were measured. This asymmetry is ascribed to the non-Schmid effect associated with screw dislocation motion (Wang and Beyerlein, 2011; Srivastava et al., 2013), and specifically to the behavior of {1 1 2} screw dislocations (Wang and Beyerlein, 2011). In addition, the activation of multiple slip planes and cross-slip in compressed pillars likely contribute to the anisotropy. Precipitates present in single-crystalline pillars may also facilitate crack initiation at high strain levels.

Plastic deformation to such high strains at room temperature is rarely achieved in either B2 materials or most BCC materials. By carefully controlling the sample size, we can examine the local deformation mechanisms within well-defined microstructures. A comparison of plastic behavior under different loading conditions, such as bending versus compression, reveals a competition between slip and cleavage mechanisms in NbMoCrTiAl (B2) samples, likely influenced by energy considerations (Takasugi et al., 1990; Yoo and Fu, 1992). Under bending or tensile loading, both slip and cleavage mechanisms occur concurrently, indicating comparable energy levels for slip and cleavage in this NbMoCrTiAl alloy. This can be rationalized by the complex compositional characteristics of CCAs: (1) studies on similar B2-type CCA systems have revealed significantly lower antiphase-boundary energies, suggesting that dislocation slip can be energetically more favorable than in conventional binary B2 alloys (Han et al., 2025; Pramanik et al., 2025; La Rosa et al., 2025; Fu and Yoo, 1990; Hong and Freeman, 1988); and (2) the intrinsic local chemical complexity in CCAs affects the local energy barriers at the crack tip, where locally reduced barriers can promote dislocation emission and plastic deformation. Therefore, cleavage does not necessarily dominate in all cases (Wang et al., 2025). These effects are more pronounced in compression, where only slip traces are observed, as cleavage is constrained, and slip is energetically more favorable. Under these conditions, cross-slip behavior was observed, contributing to additional plasticity. The slip mechanism of screw dislocations

remains dominant even at strains exceeding 40%, where cracks form around precipitates but without evidence of cleavage. The nucleation of edge segments, and consequently the formation of dislocation pathways within the ordered lattice structure, appears to be limited even for materials containing multiple principal elements and varying atomic sizes. In contrast to the TaNbHfZrTi (A2) alloy, NbMoCrTiAl samples exhibit only slip traces associated with screw dislocations. This difference accounts for the differences in plasticity observed between these two RCCA systems at the microscale.

4. Summary and conclusions

Microcantilever bending and micropillar compression tests have provided new insights into the deformation behaviors of two RCCAs, underscoring the influence of crystal structure on their mechanical response. Unlike conventional B2 alloys such as NiAl, the NbMoCrTiAl alloy demonstrated notable plastic deformation in both bending and compression experiments. This plasticity, governed solely by screw dislocation slip mechanisms, highlights the exceptional motion of screw dislocations at room temperature. The enhanced dislocation activity is likely due to local stress fields generated by the atomic size mismatch, despite the alloy's B2-ordered structure. By contrast, the BCC-structured TaNbHfZrTi alloy exhibited a broader range of deformation mechanisms, including crystallographic and non-crystallographic slip of screw dislocations, non-screw dislocations with edge segments, and kinking. Kink-pair-like dislocation features and the activation of higher-order slip plane families were also identified. The pronounced differences in deformation mechanisms, particularly in dislocation shape and the presence of edge segments, are mostly attributed to the structural differences between the ordered B2 and disordered BCC crystal structures.

Body-centered cubic CCAs provide multiple dislocation pathways, leading to an increased edge segment density, kink-pair nucleation, and enhanced dislocation motion at room temperature. This behavior is attributed to local chemical fluctuations and the random atomic distribution within the disordered crystal structure. By comparison, the B2-ordered structure of NbMoCrTiAl significantly limits these effects, resulting in a more constrained plastic deformation mechanism.

CRediT authorship contribution statement

Jin Wang: Writing – review & editing, Writing – original draft, Visualization, Validation, Methodology, Investigation, Formal analysis, Data curation, Conceptualization. **Nicolas J. Peter:** Writing – review & editing, Visualization, Investigation, Data curation. **Martin Heilmaier:** Writing – review & editing, Resources. **Ruth Schwaiger:** Writing – review & editing, Supervision, Resources, Project administration, Methodology, Funding acquisition, Conceptualization.

Declaration of competing interest

All authors declare that there are no conflicts of interest.

Acknowledgments

This research was financially supported by the Deutsche Forschungsgemeinschaft (DFG), Germany, Grant No. SCHW855/6-1 within the Priority Program SPP2006 "Compositionally Complex Alloys – High Entropy Alloys (CCA-HEA)". The sample preparation and characterization were kindly supported by Mr. Gutzeit, Ms. Esser and Dr. Wessel (IMD-1). J.W. thanks Dr. Georg Winkens for the discussion about dislocation models. This article contains results obtained from experiments performed at the Ernst Ruska-Centre (ER-C) for Microscopy and Spectroscopy with Electrons at the Forschungszentrum Jülich (FZJ) in Germany [https://doi.org/10.17815/jlsrf-2-68]. The ER-C beam-time access was provided via the [FZJ_IEK-2_NP1].

Appendix A. Supplementary data

Supplementary material related to this article can be found online at https://doi.org/10.1016/j.ijplas.2025.104593.

Data availability

Data will be made available on request.

References

Antillon, E., Woodward, C., Rao, S., Akdim, B., 2021. Chemical short range order strengthening in BCC complex concentrated alloys. Acta Mater. 215, 117012.

Armstrong, D.E., Wilkinson, A.J., Roberts, S.G., 2009. Measuring anisotropy in Young's modulus of copper using microcantilever testing. J. Mater. Res. 24 (11), 3268–3276.

Ast, J., 2016. Untersuchung der Lokalen Bruchzähigkeit und des Elastisch-Plastischen Bruchverhaltens Von Nial und Wolfram Mittels Mikrobiegebalkenversuchen (Ph.D. thesis). Erlangen, Friedrich-Alexander-Universität Erlangen-Nürnberg (FAU), Diss., 2016.

Baruffi, C., Maresca, F., Curtin, W., 2022. Screw vs. edge dislocation strengthening in body-centered-cubic high entropy alloys and implications for guided alloy design. Mrs Commun. 12 (6), 1111–1118.

Caillard, D., Gaumé, M., Onimus, F., 2018. Glide and cross-slip of a-dislocations in Zr and Ti. Acta Mater. 155, 23–34.

Charpagne, M., Stinville, J., Wang, F., Philips, N., Pollock, T., 2022. Orientation dependent plastic localization in the refractory high entropy alloy HfNbTaTiZr at room temperature. Mater. Sci. Eng.: A 848, 143291.

Chen, H., 2020. Gefüge und Eigenschaften von äquiatomaren Legierungen aus dem System Ta-Nb-Mo-Cr-Ti-Al (Ph.D. thesis). Karlsruher Institut für Technologie (KIT) - KIT-Bibliothek <90>; kostenfrei <LFER>;, Karlsruhe.

Chen, H., Hanemann, T., Seils, S., Schliephake, D., Tirunilai, A.S., Heilmaier, M., Weiss, K.-P., Kauffmann, A., 2021. Influence of temperature and plastic strain on deformation mechanisms and kink band formation in homogenized HfNbTaTiZr. Crystals 11 (2), 81.

Chen, Z., Horie, T., Wang, X., Inui, H., 2024. Operative slip systems and their critical resolved shear stresses in η-Fe2Al5 investigated by micropillar compression at room temperature. Int. J. Plast. 180, 104057.

Chen, H., Kauffmann, A., Gorr, B., Schliephake, D., Seemüller, C., Wagner, J., Christ, H.-J., Heilmaier, M., 2016. Microstructure and mechanical properties at elevated temperatures of a new Al-containing refractory high-entropy alloy Nb-Mo-Cr-Ti-Al. J. Alloys Compd. 661, 206–215.

Chen, H., Kauffmann, A., Laube, S., Choi, I.-C., Schwaiger, R., Huang, Y., Lichtenberg, K., Müller, F., Gorr, B., Christ, H.-J., et al., 2018. Contribution of lattice distortion to solid solution strengthening in a series of refractory high entropy alloys. Met. Mater. Trans. A 49, 772–781.

Chen, H., Kauffmann, A., Seils, S., Boll, T., Liebscher, C., Harding, I., Kumar, K.S., Szabó, D.V., Schlabach, S., Kauffmann-Weiss, S., et al., 2019. Crystallographic ordering in a series of Al-containing refractory high entropy alloys Ta–Nb–Mo–Cr–Ti–Al. Acta Mater. 176, 123–133.

Chou, C., Hazzledine, P., Hirsch, P., Anstis, G., 1987. Formation of antiphase-domain boundary tubes in B2 ordered alloys by cross-slip and annihilation of screw dislocations. Phil. Mag. A 56 (6), 799–813.

Cook, D.H., Kumar, P., Payne, M.I., Belcher, C.H., Borges, P., Wang, W., Walsh, F., Li, Z., Devaraj, A., Zhang, M., et al., 2024. Kink bands promote exceptional fracture resistance in a NbTaTiHf refractory medium-entropy alloy. Science 384 (6692), 178–184.

Dirras, G., Couque, H., Lilensten, L., Heczel, A., Tingaud, D., Couzinié, J.-P., Perrière, L., Gubicza, J., Guillot, I., 2016a. Mechanical behavior and microstructure of Ti20Hf20Zr20Ta20Nb20 high-entropy alloy loaded under quasi-static and dynamic compression conditions. Mater. Charact. 111, 106–113.

Dirras, G., Lilensten, L., Djemia, P., Laurent-Brocq, M., Tingaud, D., Couzinié, J.-P., Perrière, L., Chauveau, T., Guillot, I., 2016b. Elastic and plastic properties of as-cast equimolar TiHfZrTaNb high-entropy alloy. Mater. Sci. Eng.: A 654, 30–38.

Feuerbacher, M., Heidelmann, M., Thomas, C., 2015. Plastic deformation properties of Zr–Nb–Ti–Ta–Hf high-entropy alloys. Phil. Mag. 95 (11), 1221–1232.

Fu, C., Yoo, M., 1990. First-principles investigation of mechanical behavior of B2 type aluminides: FeAl and NiAl. MRS Online Proc. Libr. 213 (1), 667–672.

Gabel, S., Merle, B., 2020. Small-scale high-cycle fatigue testing by dynamic microcantilever bending. MRS Commun. 10 (2), 332–337.

Hagihara, K., Mayama, T., Honnami, M., Yamasaki, M., Izuno, H., Okamoto, T., Ohashi, T., Nakano, T., Kawamura, Y., 2016. Orientation dependence of the deformation kink band formation behavior in Zn single crystal. Int. J. Plast. 77, 174–191.

Han, S., Laube, S., Chen, Z., Kauffmann, A., Heilmaier, M., Inui, H., 2025. Operative slip system and dislocation behavior in a brittle refractory high-entropy alloy with the B2 ordered structure. J. Alloys Compd. 1020, 179361.

He, Q., Yoshida, S., Okajo, S., Tanaka, M., Tsuji, N., 2025. Characteristic dislocation slip behavior in polycrystalline HfNbTiZr refractory medium entropy alloy. J. Mater. Sci. Technol. 210, 29–39.

Hirth, J., Lothe, J., 1982. Theory of Dislocations, 1982. Wiley.

Hong, T., Freeman, A., 1988. Electronic structure and mechanical properties of intermetallics: Apb energies in Ni-Al-based systems. MRS Online Proc. Libr. (OPL) 133, 75.

Huang, W., Wang, X., Qiao, J., Shi, X., Liaw, P.K., Wu, Y., 2024. Edge dislocation-induced high-temperature strengthening in the Ti37V15Nb22Hf23W3 refractory high-entropy alloys. Mater. Sci. Eng.: A 146634.

Hunt, J.F., Zhang, H., Huang, Y., 2015. Analysis of cantilever-beam bending stress relaxation properties of thin wood composites. BioResources 10 (2), 3131–3145.

Jouybari, A.L., El Shawish, S., Cizelj, L., 2025. Enhanced Strain Gradient Crystal Plasticity theory: Evolution of the length scale during deformation. Int. J. Plast. 104351.

Kupka, D., Lilleodden, E., 2012. Mechanical testing of solid–solid interfaces at the microscale. Exp. Mech. 52 (6), 649–658.

La Rosa, L., Brodie, J., Ghazisaeidi, M., Maresca, F., 2025. Atomistic simulations reveal slip selection in B2-type intermetallic alloys. Acta Mater. 121561.

Li, W., Lyu, S., Xia, Y., Chen, Y., Ngan, A.H., 2025a. General statistical mechanics theory for fluctuating dislocation resistances in complex concentrated alloys. Int. J. Plast. 104495.

Li, Q.-J., Sheng, H., Ma, E., 2019. Strengthening in multi-principal element alloys with local-chemical-order roughened dislocation pathways. Nat. Commun. 10 (1), 3563.

Li, Z., Su, B., Liu, C., Chen, R., Wang, L., Su, Y., 2025b. Tuning deformation mechanisms in refractory high-entropy alloys: slip plane preference and dislocation behavior. Int. J. Plast. 104424.

Lilensten, L., Couzinié, J.-P., Perrière, L., Hocini, A., Keller, C., Dirras, G., Guillot, I., 2018. Study of a BCC multi-principal element alloy: Tensile and simple shear properties and underlying deformation mechanisms. Acta Mater. 142, 131–141.

Liu, Z., Chen, G., Dash, S.S., Zhou, Y., Cheng, C., Li, M., Zhang, J., Chen, H., Wang, W., Xiao, W., et al., 2025. Slip heterogeneity in a colony-structured titanium alloy: Planar versus wavy slip traces. Int. J. Plast. 104462.

Lyu, S., Li, W., Xia, Y., Chen, Y., Ngan, A.H., 2023. Effects of chemical randomness on strength contributors and dislocation behaviors in a BCC multiprincipal element alloy. Phys. Rev. Mater. 7 (7), 073602.

Lyu, S., Xia, Y., Li, W., Zhu, T., Chen, Y., Ngan, A.H., 2025. Statistical mechanics, entropy and temperature analog of dislocations moving on fluctuating resistance landscapes. Acta Mater. 291, 121002.

Maresca, F., Curtin, W.A., 2020. Theory of screw dislocation strengthening in random BCCalloys from dilute to "High-Entropy" alloys. Acta Mater. 182, 144–162.

Miracle, D., 1993. Overview No. 104 The physical and mechanical properties of NiAl. Acta Met. et Mater. 41 (3), 649–684.

Müller, F., Gorr, B., Christ, H.-J., Chen, H., Kauffmann, A., Laube, S., Heilmaier, M., 2020. Formation of complex intermetallic phases in novel refractory high-entropy alloys NbMoCrTiAl and TaMoCrTiAl: thermodynamic assessment and experimental validation. J. Alloys Compd. 842, 155726.

Philips, N., Carl, M., Cunningham, N., 2020. New opportunities in refractory alloys. Met. Mater. Trans. A 51, 3299–3310.

Pramanik, A., Konkati, C., Laube, S., Yang, L., Sen, S., Kauffmann, A., Heilmaier, M., Chauhan, A., 2025. Exploring room-temperature deformation mechanisms of a B2-strengthened refractory compositionally complex alloy. Mater. Sci. Eng.: A 931, 148180.

Riedle, J., Gumbsch, P., Fischmeister, H.F., 1996. Cleavage anisotropy in tungsten single crystals. Phys. Rev. Lett. 76 (19), 3594.

Romero, R.A., Xu, S., Jian, W.-R., Beyerlein, I.J., Ramana, C., 2022. Atomistic simulations of the local slip resistances in four refractory multi-principal element alloys. Int. J. Plast. 149, 103157.
Schmitt, N.J., 2016. Experimentelle Untersuchung Des Verformungs- Und Bruchverhaltens Von Ein-, Bi- Und Polykristallinem Wolfram Auf Der Mikroskala (Ph.D. thesis). KIT-Bibliothek, Karlsruher Institut für Technologie (KIT) - KIT-Bibliothek <90>; kostenfrei <LFER>;, Karlsruhe.
Schwaiger, R., Kraft, O., 1999. High cycle fatigue of thin silver films investigated by dynamic microbeam deflection. Scr. Mater. 41 (8), 823–829.
Seeger, A., 2022. Peierls barriers, kinks, and flow stress: recent progress. Int. J. Mater. Res. 93 (8), 760–777.
Senkov, O., Scott, J., Senkova, S., Miracle, D., Woodward, C., 2011. Microstructure and room temperature properties of a high-entropy TaNbHfZrTi alloy. J. Alloys Compd. 509 (20), 6043–6048.
Sneddon, I.N., 1965. The relation between load and penetration in the axisymmetric Boussinesq problem for a punch of arbitrary profile. Internat. J. Engrg. Sci. 3 (1), 47–57.
Srivastava, K., Gröger, R., Weygand, D., Gumbsch, P., 2013. Dislocation motion in tungsten: atomistic input to discrete dislocation simulations. Int. J. Plast. 47, 126–142.
Sun, Y., Wang, C., Ren, C., Zhang, D., Li, K., Cheung, C.F., Chen, Z., 2025. Multiscale chemical ordering heterogeneity facilitates exceptional strength and ductility in additively manufactured Ti-added AlCoCrFeNi2. 1 high-entropy alloys at intermediate temperatures. Int. J. Plast. 104373.
Takasugi, T., Hanada, S., Izumi, O., 1990. Slip modes in B2-type intermetallic alloys. Mater. Trans. JIM 31 (6), 435–442.
Thirathipviwat, P., Sato, S., Song, G., Bednarcik, J., Nielsch, K., Jung, J., Han, J., 2022. A role of atomic size misfit in lattice distortion and solid solution strengthening of TiNbHfTaZr high entropy alloy system. Scr. Mater. 210, 114470.
Wang, J., 2021. Characterization of the Size-Dependent Indentation Behavior and Dislocation Structures of Single-Crystalline Tungsten (Ph.D. thesis). Karlsruher Institut für Technologie (KIT) - KIT-Bibliothek <90>; kostenfrei <LFER>;, Karlsruhe.
Wang, F., Balbus, G.H., Xu, S., Su, Y., Shin, J., Rottmann, P.F., Knipling, K.E., Stinville, J.-C., Mills, L.H., Senkov, O.N., Beyerlein, I.J., Pollock, T.M., Gianola, D.S., 2020a. Multiplicity of dislocation pathways in a refractory multiprincipal element alloy. Science 370 (6512), 95–101.
Wang, J., Basu, S., Kauffmann, A., Heilmaier, M., Schwaiger, R., 2024a. The effect of grain boundaries and precipitates on the mechanical behavior of the refractory compositionally complex alloy NbMoCrTiAl. Appl. Phys. Lett. 124 (20).
Wang, Z., Beyerlein, I., 2011. An atomistically-informed dislocation dynamics model for the plastic anisotropy and tension–compression asymmetry of BCC metals. Int. J. Plast. 27 (10), 1471–1484.
Wang, Y., He, Q., Ye, Z., Liao, Y., Li, C., Wang, Q., Gu, J., 2024c. Ductilization of single-phase refractory high-entropy alloys via activation of edge dislocation. Acta Mater. 120614.
Wang, W., Kumar, P., Cook, D.H., Walsh, F., Zhang, B., Borges, P.P., Farkas, D., Ritchie, R.O., Asta, M., 2025. Ductility mechanisms in complex concentrated refractory alloys from atomistic fracture simulations. Npj Comput. Mater. 11 (1), 330.
Wang, T., Li, J., Wang, M., Li, C., Su, Y., Xu, S., Li, X.-G., 2024b. Unraveling dislocation-based strengthening in refractory multi-principal element alloys. Npj Comput. Mater. 10 (1), 143.
Wang, J., Luan, L., Volz, T., Weygand, S.M., Schwaiger, R., 2022. Size-dependent geometrically necessary dislocation structures in single-crystalline tungsten. J. Mater. Res. 37 (21), 3646–3657.
Wang, S., Wu, M., Shu, D., Zhu, G., Wang, D., Sun, B., 2020b. Mechanical instability and tensile properties of TiZrHfNbTa high entropy alloy at cryogenic temperatures. Acta Mater. 201, 517–527.
Xu, S., Su, Y., Jian, W.-R., Beyerlein, I.J., 2021. Local slip resistances in equal-molar MoNbTi multi-principal element alloy. Acta Mater. 202, 68–79.
Yoo, M., Fu, C., 1992. Cleavage fracture of ordered intermetallic alloys. In: High Temperature Aluminides and Intermetallics. Elsevier, pp. 470–478.
Zhai, J.-H., Zaiser, M., 2019. Properties of dislocation lines in crystals with strong atomic-scale disorder. Mater. Sci. Eng.: A 740, 285–294.
Zhang, H., Schuster, B.E., Wei, Q., Ramesh, K.T., 2006. The design of accurate micro-compression experiments. Scr. Mater. 54 (2), 181–186.
Zhang, L., Xiang, Y., Han, J., Srolovitz, D.J., 2019. The effect of randomness on the strength of high-entropy alloys. Acta Mater. 166, 424–434.
Zherebtsov, S., Yurchenko, N., Shaysultanov, D., Tikhonovsky, M., Salishchev, G., Stepanov, N., 2020. Microstructure and mechanical properties evolution in HfNbTaTiZr refractory high-entropy alloy during cold rolling. Adv. Eng. Mater. 22 (10), 2000105.
Zhou, X., Wang, X., Fey, L., He, S., Beyerlein, I., Cao, P., Marian, J., 2023. Models of dislocation glide and strengthening mechanisms in BCC complex concentrated alloys. MRS Bull. 48 (7), 777–789.